Monterey Bay Aquarium
Research Institute

# Characterizing a Moderately Priced IMU to Determine Viability for Coastal Profiling Float Drift Mitigation

**Reyna Ayala, Massachusetts Institute of Technology**

***Mentor: Gene Massion***

***Summer 2023***

## ABSTRACT

Profiling floats have proven invaluable in acquiring long term, synoptic and comprehensive data sets important to understanding the health of the ocean. Moving profiling float technology into the equally important coastal ocean requires an ability to mitigate a float drifting out of the desired measurement volume. While a costly navigation system remains a possible solution, this project investigates the lower limit of detection of a moderately priced inertial measurement unit (IMU) to determine its viability for estimating ocean current velocities from acceleration measurements. A rotary test table was designed to impose known and controllable accelerations to the sensor. Since bias and misalignment corrections inherent in any IMU application were beyond the project scope, signals remained uncalibrated. Though, the results still pointed to a likely value for the lower limit of acceleration detection. Given this estimated lower limit, the accelerations relevant to float drift mitigation were out of the selected sensor's detectable range without the additional work required to correct for drift and misalignment.

# INTRODUCTION

Coastal marine environments refer to regions interfacing between land and the open ocean and are typically defined as the waters over the continental shelf. Scientific observation of coastal waters is distinctly important to studies monitoring anthropogenic climate change given large fluxes of carbon-based compounds occurring between the land and ocean.[1,8] Further underlining the importance of their study, coastal regions are most vulnerable among marine environments to pollutant runoff.[6]

Despite the unique conditions and importance of coastal phenomena, these waters have largely been under-sampled. Shallow depths, steep temperature and density gradients, and strong tidal currents present in coastal waters introduce significant engineering challenges for teams aiming to design and implement profiling technologies.[10]

Among existing profiling technologies are devices called floats that house biogeochemical sensors. Profiling floats feature depth control, filling and emptying external bladders with oil to manipulate buoyancy force.[5] Floats lack positional control and are expected to drift with ocean currents, particularly when transmitting data at surface level, where winds will drive currents. CPF displacement introduces the risk of excessive drift onshore or offshore.[9]

For many coastal zones, the typical surface current is generally accompanied by an opposing current at a lower depth.[7] By measuring ocean current dynamics throughout a float's vertical profile, a current velocity vs. depth profile can be calculated. With this data, the float could select a depth at which to park, "navigating" back into the desired measurement volume.

Dominant methods of ocean current velocity sensing rely on a fixed Eulerian reference frame. However, floats are designed to move with ocean currents, requiring a Lagrangian approach.[8] The MBARI Chemical Sensor Lab has tried using computational ocean current models to predict depths with desired velocities for CPF displacement correction. This method did not satisfy drift minimization requirements, prompting exploration of onboard ocean current sensing options which require lower accuracy given a dependence on live measurements rather than predictions values.

Open ocean profiling floats proved most informative when participating in a global network, as suggested by the successes of the Argo program and GO-BGC initiative.[5] CPFs are not as widespread as open ocean floats due to additional aforementioned engineering challenges. To eventually achieve a larger network of coastal profiling floats, design and operational costs must remain low to support the accessibility of CPF projects. In addition, power consumption and physical space are critical metrics for float success. These requirements drive the choice of onboard current sensing technique towards low power, volume and cost.[9]

Since acceleration data can be numerically integrated to estimate velocity, a moderately priced inertial measurement unit (IMU) was considered for an onboard current sensor. Acceleration measurement allows for current velocity estimation while in a Lagrangian reference frame. IMU devices feature both magnetometers and accelerometers, allowing for accelerations to be measured with respect to the North-East-Down (NED) frame. As CPFs may experience slight shifts in orientation, the NED frame is useful in the ocean. To use the North-East-Down reference frame, the IMU's magnetometer must be calibrated. Although the CPF would use the NED frame, magnetometer calibration was out of scope for this internship.

The primary objective of this project was to determine the feasibility of implementing the VN-100 VectorNav IMU to estimate linear velocities of ocean currents in order to mitigate CPF drift. To ascertain whether the sensor could measure accelerations imposed on the CPF, the sensor's lower limit of acceleration detection required identification.

# MATERIALS AND METHODS

## DESIGN REQUIREMENTS

Determining whether the VN-100 IMU could adequately estimate ocean current velocities required an understanding of typical and extreme ocean current dynamic profiles. This established a framework around which to design a physical method for sensor testing.

While the CPF would utilize velocity vs. depth estimations in selecting a parking depth, the IMU could not directly measure linear velocities, but instead linear accelerations. Thus, IMU viability depended on detectable acceleration signals. To characterize possible accelerations that a CPF may encounter, numerical differentiation methods were applied to ocean current velocity versus depth profiles collected in 1998 by the Ocean Acquisition System for Interdisciplinary Science.[2] In cases of both typical and extreme ocean currents, the acceleration order of magnitude relevant to CPF application was 10^-4 m/s^2. To determine IMU viability, accelerations of this order needed to be inducible by a test bed.

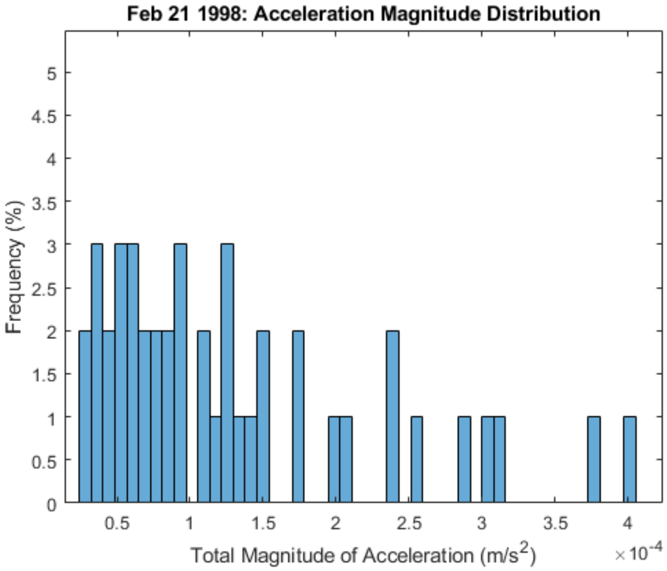

**Figure I** (above): Example of typical ocean current profile acceleration distribution. Leftmost bin was excluded from histogram, as values were assumed zero.

To adequately characterize the VN-100 IMU, known and controllable accelerations must be achievable. A test bed was also required to maintain, as needed, a specified acceleration for prolonged periods.

Additive white Gaussian noise demands relatively simple signal processing methods to be eliminated from the signal. Mechanical vibrations do not follow Gaussian distributions and thus require more complex filtering. With the intent of measuring accelerations of such small orders of magnitude, vibration elimination proved a crucial design consideration.

These test bed criteria were summarized into the following design requirements:

1) Accelerations on the order of 10^-4 m/s^2 must be achievable to impose on the IMU.
2) The test bed must be able to apply known, controllable accelerations to the sensor over a prolonged period of time. This includes the ability to impose a constant acceleration.
3) The design must feature vibration elimination strategies, considering static and dynamic imbalances, backlash, and vibration sources external to the test bed system.

## DESIGN CONCEPTS & PRELIMINARY DESIGN

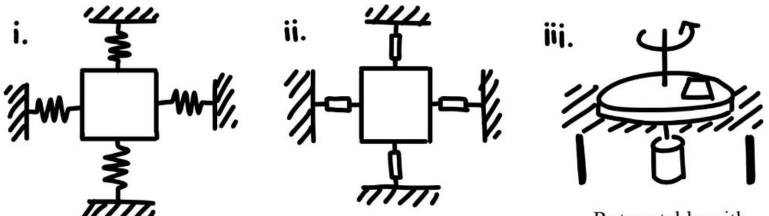

Linear spring table

Hydraulic or Pneumatic Linear Actuators

Rotary table with vibration mounts

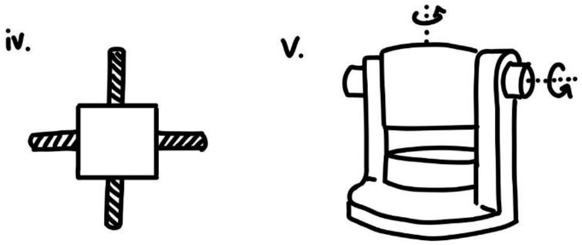

Threaded rod table

Multi-axis rotary table

**Figure II** (left): Illustrated concepts for controlled acceleration mechanism.

Initially, the preceding concepts were devised as methods of imposing a known and controllable acceleration on the sensor.

The single-axis rotary table with vibration mounts was selected. Concepts that applied translational motion required excessively long linear paths if aiming to apply a constant acceleration over a significant period of time. Although rotational motion did not replicate motion experienced by CPFs, it could apply a constant centripetal acceleration for unlimited time. For the purposes of determining the lower limit of acceleration detection, designing a test bed to apply centripetal rather than translational accelerations was acceptable. Furthermore, motor control achieves more precise control than linear hydraulic, pneumatic, or spring actuators. Finding the lower limit of detection did not necessitate testing about more than one axis, eliminating the multi-axis rotary table concept.

After developing designs for a low-vibration rotary table, two designs stood out as promising options. The primary distinction between these concepts was motor placement: whether to mount the motor along the same shaft driving the rotating table or to decouple the motor with a belt or gear power transmission.

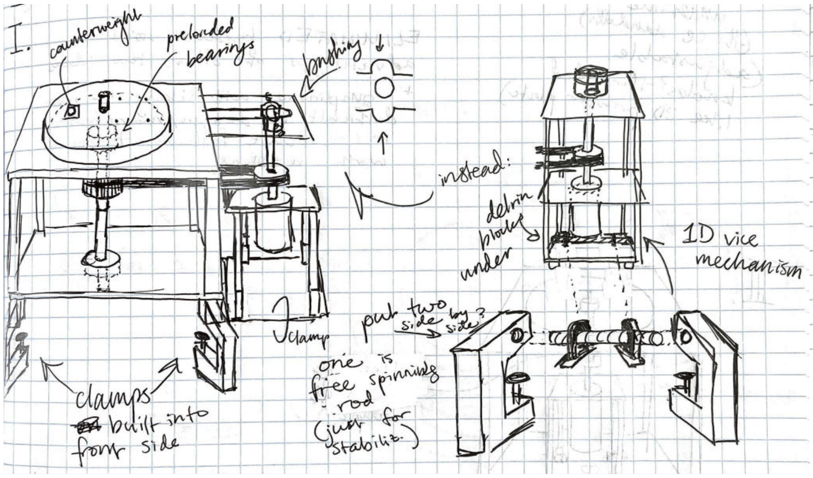

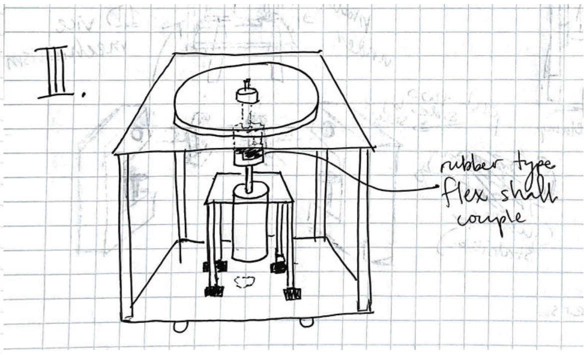

**Figure III**: Developed concepts.

Despite the relative simplicity of directly driving the rotating table with a flexible shaft coupling, its limited capacity for adjusting transmission ratio was deemed a significant design risk. Transmission ratio adjustments in this design required either a custom gear train or new equipment, introducing risks of additional backlash and cost, respectively. As such, the decoupled motor mount concept was selected with modifications to simplify manufacturing and reduce vibrations.

Motors inevitably produce mechanical noise, particularly with multi-stage gearheads installed.[4] Separation of the motor module isolated motor-induced mechanical noise from the rotating table. A fixed distance of separation between the motor and rotating table shafts was required to preserve the adjustable belt tension feature. To achieve both motor isolation and a fixed distance of separation, a base plate was introduced. The base plate replaced the original idea to clamp onto an external surface, which would have introduced noise from surrounding activity.

Additional strategies were implemented to reduce vibrations, as listed below.

1. A counterweight mounted symmetrically to the sensor and of equivalent mass adequately addressed the risk of static imbalance of the rotating table.
2. Using a timing belt drive instead of a gear train for power transmission avoided backlash associated with rigid gear teeth. Timing belts mostly evade issues with pulley slip. A properly tensioned timing belt will also absorb some amount of vibrations as a result of their rubber material composition.
3. The number of unsupported spans present in each part of the assembly was minimized when deciding where to place standoff supports.

4. Rubber vibration mounts were implemented between any mounting interface that could otherwise transmit vibrations between modules.
5. Flexible rubber-insert shaft couplings replaced rigid shaft couplings. As an added advantage, the flexible rubber-insert shaft couplings compensated for any potential sources of misalignment overconstraint applied to the shafts.

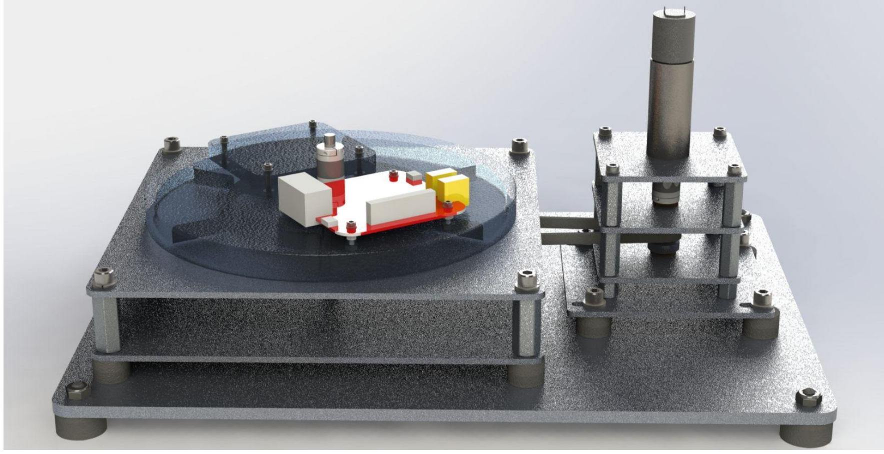

**Figure IV** (above): High-resolution rendered CAD model of preliminary design

**Figure V** (below): Annotated CAD assembly drawing

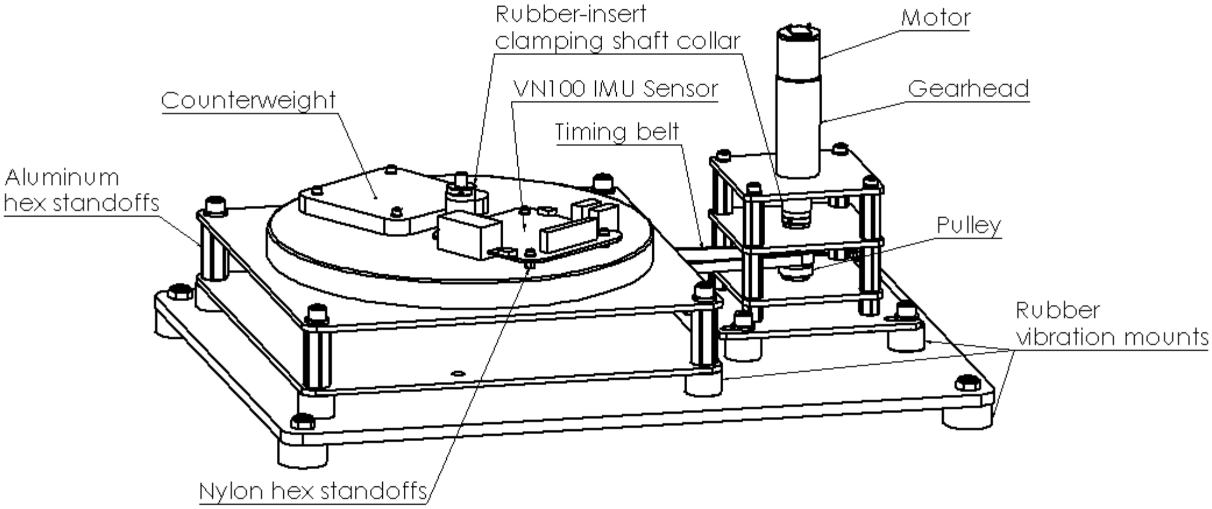

A 5647:1 gearhead on the 1724T024SRIEH2-4096+16/7 Faulhaber motor and 3:1 (60:20) pulley ratio were selected to achieve the desired acceleration order of magnitude.

# FINAL DESIGN

Accelerations at the desired order of magnitude were in range of the original motor and gearhead chosen, but the installed encoder exhibited no detectable signal during motor operation. Initial wiring mistakes likely induced an electrical short on the encoder. At that time, it was unrealistic to delay data collection by the time required to exchange the device. Thus, an alternate motor owned by the laboratory, 2224U012SRIE2-16+23/1 1526:1+MG13 by Faulhaber, was interchanged with the original.

If the angular speed range achievable by the motor, gearhead, and pulley configurations fell below the range of detectable accelerations, it would be necessary to verify the lower limit of detection by imposing higher speeds. Consequently, 18-tooth and 72-tooth pulleys of 2.3mm pitch were acquired. After testing multiple configurations of the 18, 20, 60, and 72 toothed pulleys, a 18:72 pulley tooth overdrive ratio was selected for the final design, as live signals observed in this configuration seemed most promising. The resulting overall speed reduction between the motor and table was 763:2.

The planned mounting of the 3D printed table to the output shaft involved bolting one side of a rubber-insert shaft coupling to the table and clamping the remaining side to the shaft. However, the shaft coupling was deformed when milling and tapping threaded attachment holes. The resulting angled mount created a dynamic imbalance causing significant vibration. Consequently, a rigid shaft collar with threaded attachment holes replaced the original rubber-insert shaft coupling method.

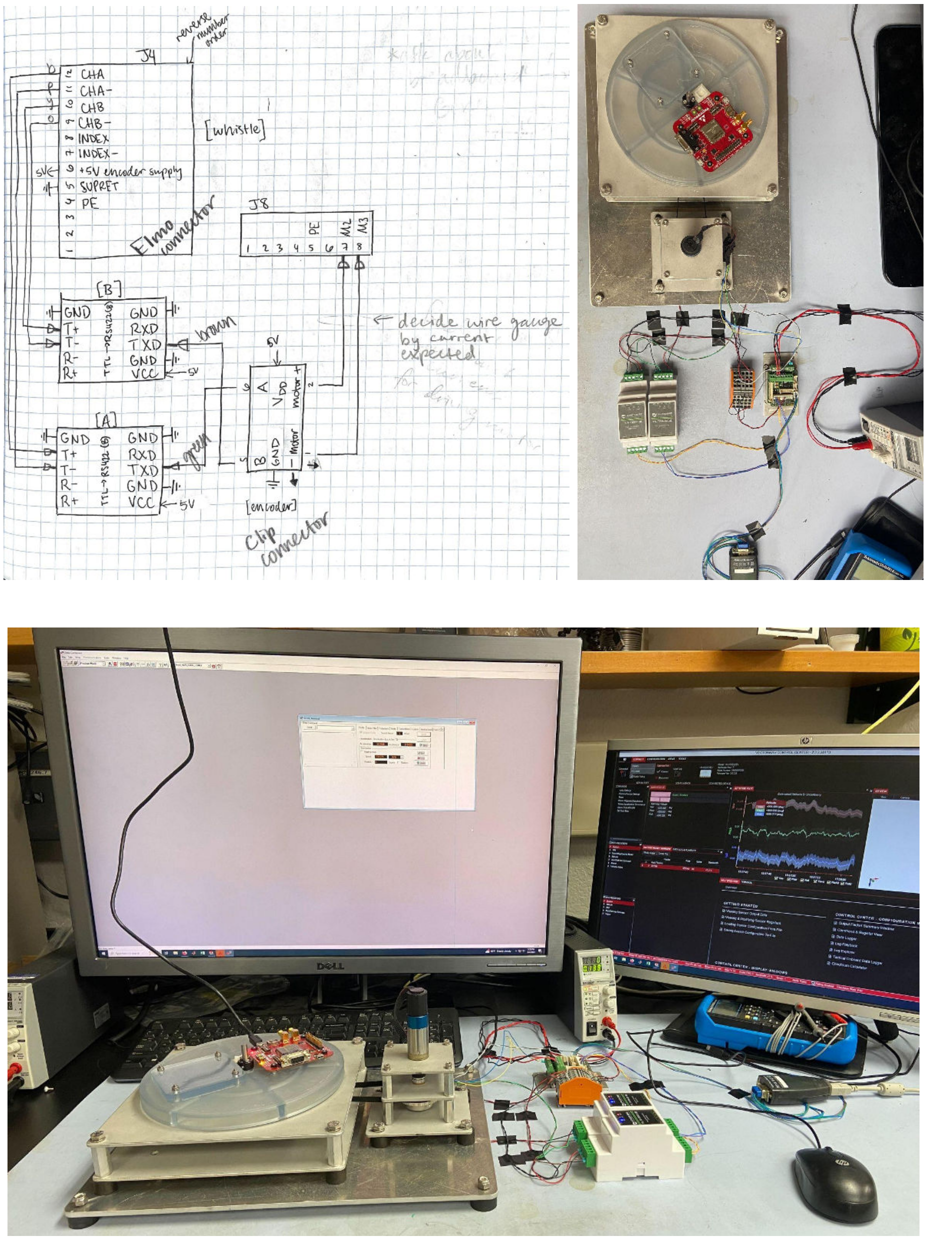

**Figure VI**: Topmost images display electrical schematic and implementation. Bottom image includes rotary test table assembly with Elmo Composer and VectorNav Control Center displayed on monitors.

## SERVO DRIVER CONTROL LOOP TUNING

The Elmo Solo Whistle 5/60 was used as a servo driver to the selected motor. During initial functionality testing of the motor, the Elmo Composer software continued to display an “over speed” error, regardless of commands applied to the device. Elmo Composer required use of a proportional-integral (PI) controller for velocity control. To reveal gains that may allow the plant-controller closed loop transfer function to stabilize, a mathematical model of the rotary table was developed. The model neglected to consider armature resistance, damping, and motor shaft stiffness, as their effects were assumed to be negligible.

$k_t$: torque constant, $1.3655\ Nm/A$

$V$: time-varying input voltage, $V$

$L_a$: inductance, $8 * 10^{-4}\ H$

$J_1$: rotor inertia, $2.6 * 10^{-7}\ kg * m^2$

$J_2$: load inertia, $0.001\ kg * m^2$

$i$: time-varying input current, $A$

ω: rotor angular speed, $rad/s$

Ω: rotating table speed, $rad/s$

$n$: combined gear ratio

$$V - k_t \omega = L_a \frac{di}{dt}$$

$$J_1 \frac{d\omega}{dt} = k_t i$$

$$\Omega = n * \omega$$

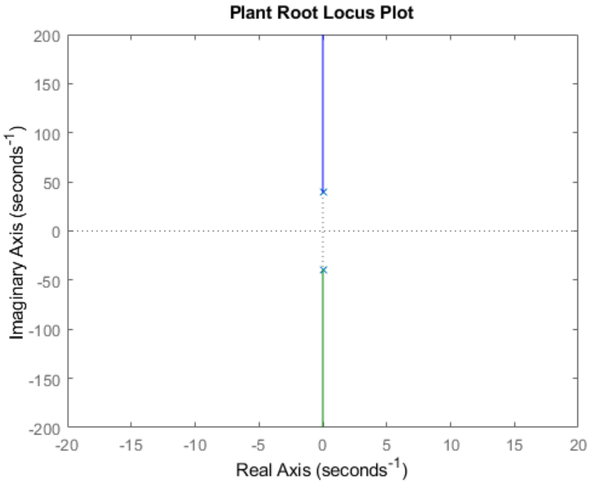

**Figure VII** (above) : Plant root locus plot.

Plant transfer function: $\dfrac{\Omega}{V} = \dfrac{n^* k_t}{L_a (J_1 + J_2)^* s^2 + k_t^2} = \dfrac{1118.2}{s^2 + 1527}$

Figure VI revealed that a PI controller would not stabilize the system regardless of gain. After reviewing the controller options available in Elmo Composer, a lead compensator was added to the required PI controller, successfully stabilizing velocity control of the system.[3]

Controller transfer function: $\frac{K_p(s+K_i)(s+z_1)}{s\,(s+p_1)} = \frac{41.169\,(s+49.86)(s+35)}{s\,(s+200.6)}$

**Figure VIII** (right): Plant and controller root locus plot.

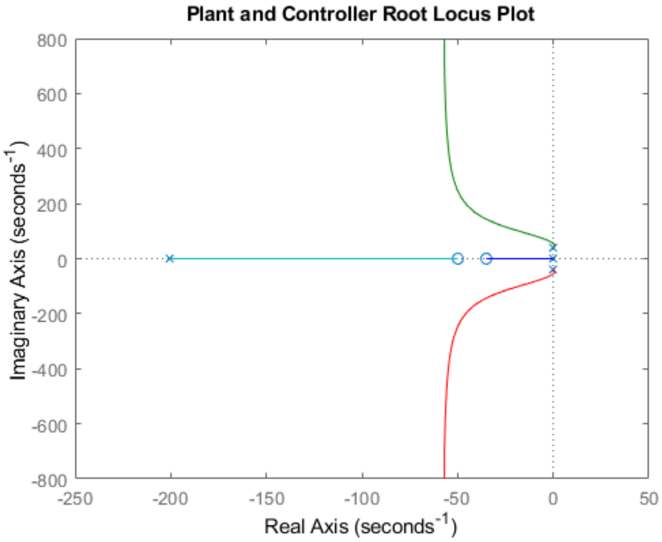

**Figure IX** (below, left): Modeled unit step response of closed-loop plant and controller.

**Figure X** (below, right): Measured motor speed vs. time when commanded to 3000 rpm.

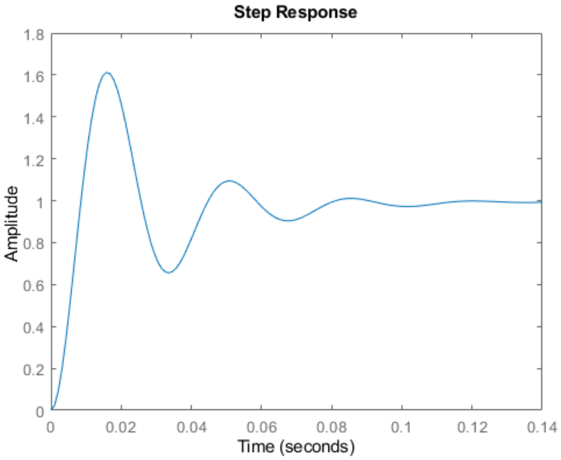

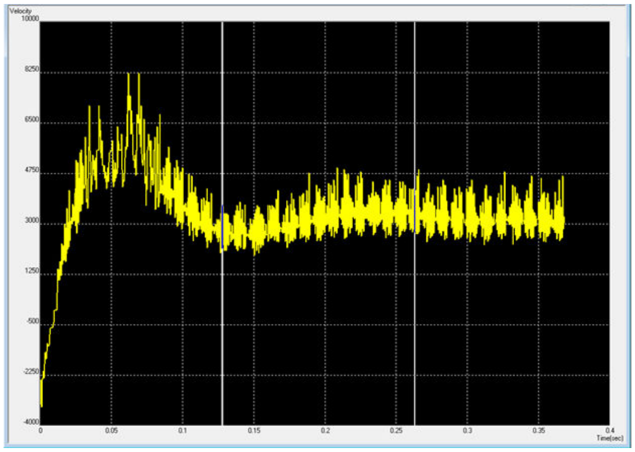

## TEST PLAN

The following sequence of operations was performed with motor angular speed commands set to 3000, 2500, 2000, 1750, 1500, 1000, and 500 rpm.

1. The desired motor angular speed value (rpm) was set in the Elmo Composer application in “Velocity Mode”. Once the encoder reported reasonably stable values around the desired angular speed, the VectorNav Command Center data logger was started,

recording values in binary outputs[1]. The data logger was manually stopped after no less than three full periods.

2. With the logged data, a MATLAB script plotted both:
   a. Unfiltered, uncompensated linear acceleration in the x-direction vs. time
   b. The frequency-normalized Welch power spectral density of the unfiltered, uncompensated linear acceleration signal in the x-direction
3. An FIR filter of order 200 using a Chebyshev window with cutoff frequency 0.02 (frequencies normalized to 1) and sidelobe attenuation of 50 was applied to the unfiltered acceleration data.
4. Two more plots were generated:
   a. Filtered, uncompensated linear acceleration in the x-direction, $a_x$, vs. time. This plot also displayed a line along the mean acceleration value of the signal, $a_{x,mean}$.
   b. The frequency-normalized Welch power spectral density of the filtered, uncompensated linear acceleration signal in the x-direction.
5. An angular speed vs. time graph was generated, displaying:
   a. Estimated ω from acceleration average: a line along the theoretical motor speed associated with $a_{x,mean}$ by the relation $a = \Omega^2 r = (n\omega)^2 r$ [Equation I.]
   b. Estimated ω of each acceleration point: a plot of the theoretical motor speed command associated with each point in the $a_x$ signal via Eqn. I.
   c. Mean of estimated ω's: a line along the mean value of (b) estimated ω's of each acceleration point.

---

[1] The VectorNav Command Center offers two output types: ASCII and binary. This study demanded uncompensated acceleration values in order to avoid extraneous frequencies from the built-in Kalman filter. ASCII outputs are solely compensated, so binary outputs were chosen.

d. Actual ω: gyroscope measurements with respect to the z-axis, scaled to account for the gear reduction between the motor and rotating table.

To validate previous results, two tests with the following motor commands were individually performed:

1. The data logger was started while the motor was stationary, at 0 rpm. The acceleration rate was set to 100 counts per second-squared. A command was sent to the Elmo Solo Whistle servo driver via Elmo Composer to accelerate to 3000 rpm. When compared with gyroscope readings, this test would theoretically validate the speed (and associated centripetal acceleration) at which the acceleration signal leaves the noise floor.
2. The data logger was started while the motor was at 3000 rpm. The acceleration and deceleration rates were set to 10000 counts per second-squared to achieve near-instant speed change. After running for a few full table rotations, the motor was accelerated to -3000 rpm. The lowest magnitude point where the signal surpassed the extrema of the noise floor would verify the lower limit of detection.

## RESULTS

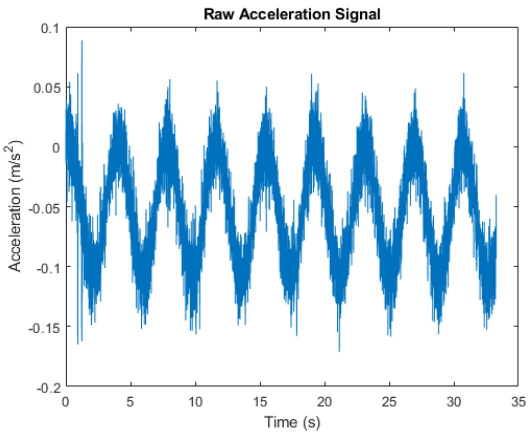

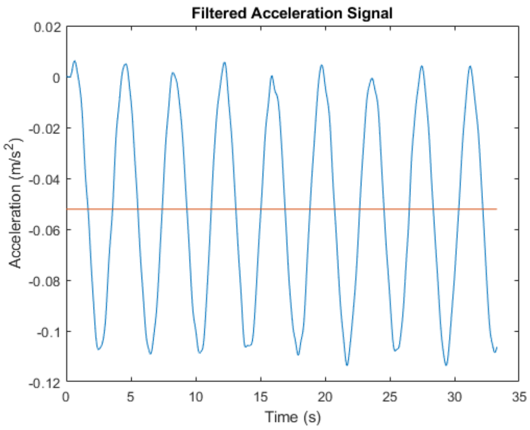

**Figure X** (above): Unfiltered and filtered uncompensated x-direction acceleration signals with motor command speed of 3000 rpm.

**Figure XII** (right): Angular speed vs. time, as described in step 6 of the test plan.

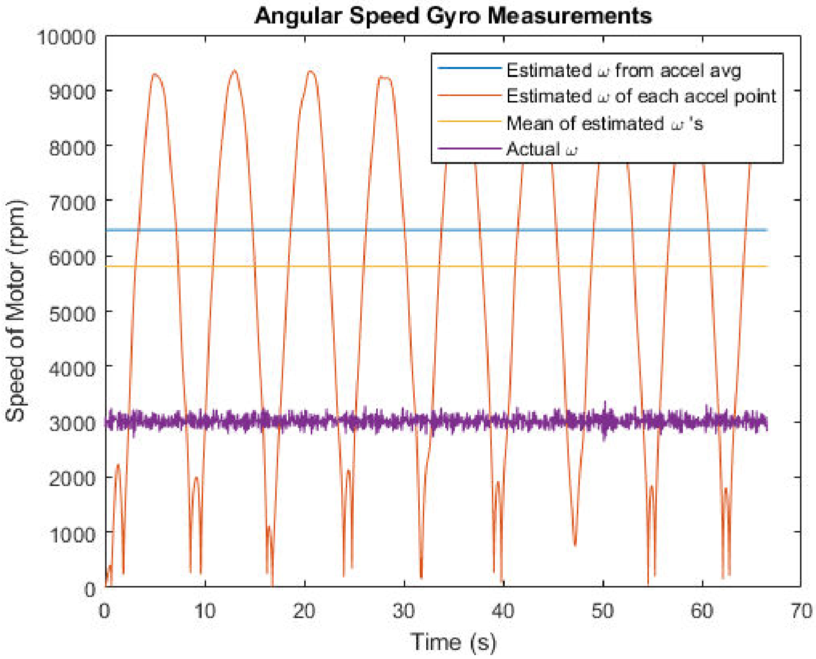

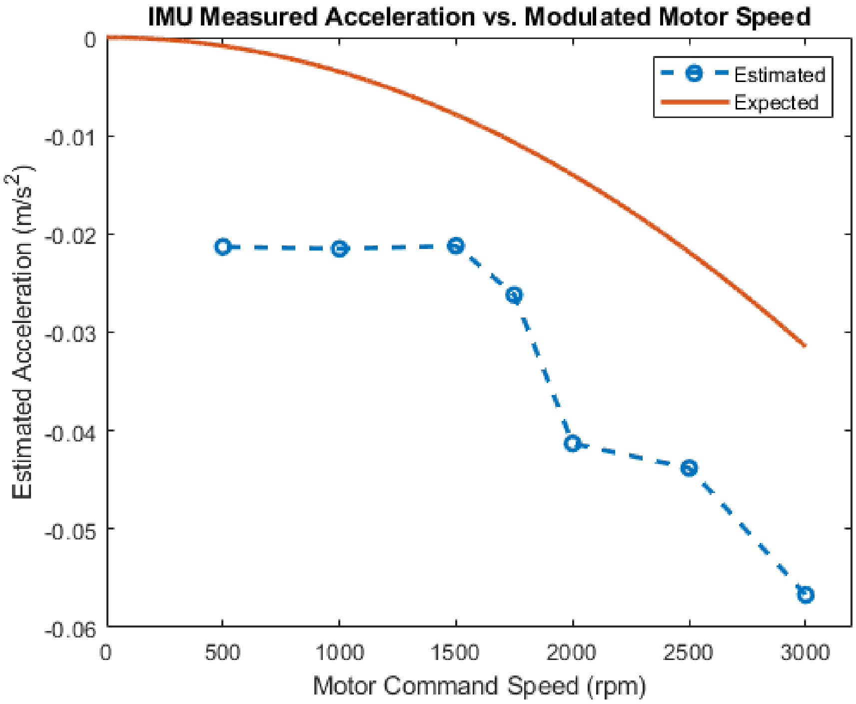

**Figure XIII** (left): Estimated points refer to acceleration mean values, $a_{x,mean}$, calculated from measured accelerations given motor command speeds. Expected values are calculated with Eqn. I.

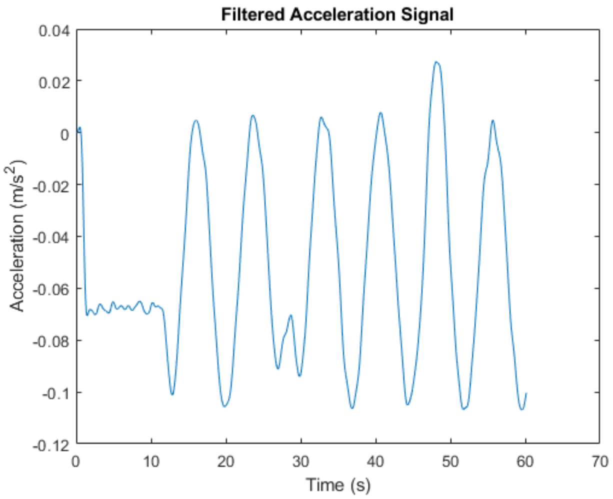

**Figure XV** (right): Filtered acceleration signal vs. time of the 0 to 3000 rpm motor speed command test.

**Figure XIV** (left): Filtered acceleration signal vs. time of the 3000 to -3000 rpm motor speed command test.

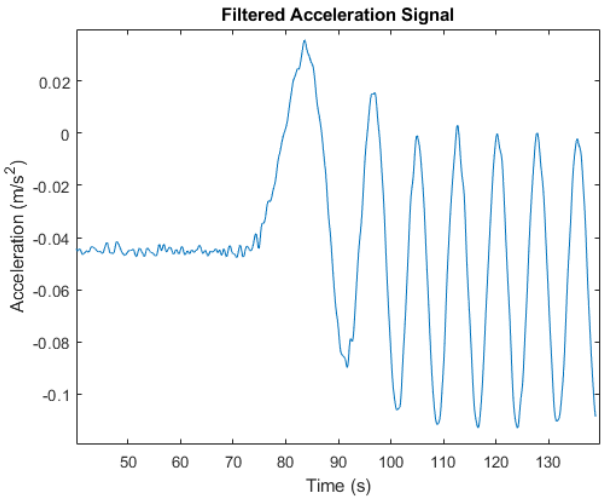

## DISCUSSION

The results of tests conducted with the rotary table suggested that the lower limit of acceleration detection of the VN100 IMU sensor was likely about 0.01 $m/s^2$, though further testing is required due to discrepancies between measurements and expected system dynamics. The sensor was mounted to align its theoretical origin with the center of rotation. An ideal model would exhibit a centripetal acceleration signal of constant amplitude in the x-direction. Figure X demonstrated that the acceleration signal in the x-direction was periodic, revealing the presence of misalignment errors. Possible sources of misalignment included the true sensor x-axis failing to intersect the center of rotation and the degree to which the sensor was level.

Sensor bias and misalignment introduced significant error. As seen in Figure VIII, the estimated ω from the acceleration mean and the mean of estimated ω's both differed from the actual ω by roughly a factor of two. Furthermore, the mean value of unfiltered, uncompensated acceleration data at a motor speed command of zero was inconsistent, suggesting a complexity in bias compensation that exceeded the scope of the internship. This realization rendered Figures XIV and XV inconsequential; without proper sensor calibration, the acceleration magnitudes at which the signal left the noise floor did not represent the actual lower limit of detection.

The significant offset in Figure XIII between measurement-based estimations and expected centripetal accelerations associated with motor speeds via Eqn. I further suggested that a lower limit of detection value could not be interpreted directly. The curve representing expected centripetal accelerations did demonstrate that the accelerations imposed by motor command speeds of 1500 rpm versus 500 rpm should have been significantly different, revealing an inconsistency with observed results. The sensor did not distinguish between motor speed commands from 500 to 1500 rpm. The first distinguishable estimated acceleration occurred at 1750 rpm to the motor, indicating that the lower limit of detection occurred near this angular speed. Although the estimated acceleration value was based on uncalibrated measurements, Eqn. I allowed the true lower limit of detection to be estimated at 0.01 $m/s^2$. Since the acceleration order of magnitude relevant to CPF application was $10^{-4}$ $m/s^2$, a lower limit of detection estimation of 0.01 $m/s^2$ suggested that the VN100 IMU will not adequately detect ocean current accelerations for velocity estimation.

## CONCLUSION

This project aimed to determine the viability of the VN100 IMU sensor in estimating ocean current velocities using acceleration measurements as a means of mitigating CPF drift. To inform viability, the lower limit of acceleration detection required investigation, prompting the design of a rotary table able to impose known and controllable accelerations on the IMU. Comparing expected accelerations versus measurement-based estimates revealed the point at which the sensor did not report significantly different accelerations for motor speeds that should have been distinguishable if trends from higher speeds had continued. This point, observed at about 1750 rpm, suggested that the lower limit of detection was likely about 0.01 $m/s^2$. Although bias compensation and misalignment corrections are required to perform tests validating this result, the estimated lower limit indicated that the VN100 is not suitable for CPF drift mitigation.

## ACKNOWLEDGEMENTS

Thank you to Gene Massion for his mentorship and enthusiastic guidance throughout the project and internship program. Thank you to George Matsumoto for his leadership of the intern program and his continued support throughout the summer. Thank you to Roman Marin, Evan Mattiasen, and Aaron Schnittger for their support in manufacturing parts and willingness to teach machine shop skills. Thank you to Jose Rosal and Jim Montgomery for their assistance with electrical wiring skills. Thank you to Giancarlo Troni and Sebastian Rodriguez for offering invaluable insights on IMU calibration and output data types.

## References:

(1) Charette, Matthew A, et al. "Coastal Ocean and Shelf-Sea Biogeochemical Cycling of Trace Elements and Isotopes: Lessons Learned from GEOTRACES." *Philosophical Transactions Royal Society A*, vol. 374, 2016, https://doi.org/10.1098/rsta.2016.0076.

(2) "Daily Averaged OASIS Data Sets." *MBARI*, 1998, Accessed June 2023.

(3) Franklin, Gene F, et al. *Feedback Control of Dynamic Systems*. 8th ed., Pearson, 2019.

(4) Gonzalez, Patxi, et al. “Noise in Electric Motors: A Comprehensive Review.” *Energies*, vol. 16, no. 14, 11 July 2023, p. 5311, https://doi.org/10.3390/en16145311.

(5) Johnson, K.S., W.M. Berelson, E.S. Boss, Z. Chase, H. Claustre, S.R. Emerson, N. Gruber, A. Körtzinger, M.J. Perry, and S.C. Riser. “Observing Biogeochemical Cycles at Global Scales with Profiling Floats and Gliders: Prospects for a Global Array.” *Oceanography*, vol. 22, no. 3, 2009, pp. 216–225, https://doi.org/10.5670/oceanog.2009.81.

(6) National Oceanic and Atmospheric Administration. “What Is the Biggest Source of Pollution in the Ocean?” *NOAA's National Ocean Service*, 8 Oct. 2008, oceanservice.noaa.gov/facts/pollution.html.

(7) “Ocean Surface Currents.” *Exploring Our Fluid Earth*, manoa.hawaii.edu/exploringourfluidearth/physical/atmospheric-effects/ocean-surface-currents. Accessed 10 Aug. 2023.

(8) Siefert, Ronald L., and Gian-Kasper Plattner. “The Role of Coastal Zones in Global Biogeochemical Cycles.” *Eos, Transactions American Geophysical Union*, vol. 85, no. 45, 9 Nov. 2004, p. 470, https://doi.org/10.1029/2004eo450005.

(9) Smith, Ryan N, and Van T Huynh. “Controlling Buoyancy-Driven Profiling Floats for Applications in Ocean Observation.” *IEEE Journal of Oceanic Engineering*, vol. 39, no. 3, July 2014, pp. 571–586, https://doi.org/10.1109/joe.2013.2261895.

(10) Vinothkumar, Viswanathan, and Taher Tawfiq. “Buoyancy Driven Autonomous Profiling Float for Shallow Waters.” IEEE, 2016.